PHYSICAL REVIEW A **88**, 012904 (2013)

Surface-grating deflection of fast atom beams

A. Zugarramurdi,[1] M. Debiossac,[1] P. Lunca-Popa,[1] L. S. Alarcón,[2] A. Momeni,[1,3] H. Khemliche,[1]
P. Roncin,[1] and A. G. Borisov[1]
[1]*Institut des Sciences Moléculaires d'Orsay, ISMO, UMR 8214 CNRS-Université Paris-Sud, Bât. 351,*
Université Paris-Sud, 91405 Orsay CEDEX, France
[2]*Centro Atómico Bariloche, CNEA, I. Balseiro, UNC & CONICET, Bustillo 9500, R8402AGP Bariloche, Argentina*
[3]*Université de Cergy-Pontoise, 33 Boulevard du Port, F-95031 Cergy, France*

(Received 7 May 2013; published 29 July 2013)

For energetic atomic beams grazingly incident at the surface along the low index directions, fast motion parallel to the surface and slow motion perpendicular to the surface lead to the quantum diffraction pattern in the scattered beam. In this experimental and theoretical joint study we show that when the incident beam is misaligned with respect to an axial channel, the characteristic deformation of the diffraction pattern reflects an overall deflection of the scattered beam from the specular direction. The deflection is maximum for the azimuthal misalignment angles close to the rainbow angle and we show how this effect can be explained with the detailed balance principle relating diffraction of misaligned and perfectly aligned beams. We also demonstrate that using the detailed balance principle the diffraction charts for the incident beams aligned along the axial channel can be reconstructed from the azimuthal incidence angle dependence of the data obtained with misaligned beams.

DOI: 10.1103/PhysRevA.88.012904 PACS number(s): 34.35.+a, 34.50.Cx, 68.49.Bc

I. INTRODUCTION

Interaction of swift particle beams with solid surfaces has been thoroughly studied over the decades because of the fundamental and practical interest. Developed analytical and numerical tools successively explain scattering and sputtering experiments within the classical framework of transport and collision theories [1–4]. Indeed, the small de Broglie wavelength of the projectile, as well as electron and phonon excitations produced upon impact at surfaces, would be the arguments for the classical behavior. In this respect, recent observation of fast atom diffraction at monocrystal surfaces upon grazing incidence [5–10] demonstrated that energy losses and associated decoherence can be made small [11–13] leading to the quantum behavior of the projectile beam. Observed well-resolved diffraction patterns in the scattered beam opened an avenue for the application of this technique as a powerful tool for surface analysis [10,14,15]. The diffraction is possible because, under grazing angles, the de Broglie wavelength associated with the slow projectile motion perpendicular to the surface is comparable to interatomic spacings at the surface.

Observation of grazing incidence fast atom diffraction at surfaces (FAD, also referred to as GIFAD) prompted numerous experimental and theoretical studies [7–12,16–18] mainly addressing the case of the incident beam being perfectly aligned along a low index direction at the surface. Here we address the much less studied case where the incident atom beam is misaligned with respect to the low index direction at the surface. While for large misalignments the diffraction is suppressed and planar surface channeling with specular reflection is retrieved [10,19,20], the case of the small misalignment allows us to observe the guiding and beam deflection effects. Our experimental and theoretical results for FAD of ^{4}He projectiles from the LiF(001) surface show controllable beam deflection in the direction of atomic rows forming an axial channel (grating structure) at the surface. Along with overall deflection of the beam, for specific azimuthal incidence angles close to the rainbow angle efficient perfect alignment can be reached where the intense diffracted beam leaves the surface exactly following the low index direction. Our results suggest that the surface scattering at grazing angles can be used for coherent manipulation of fast atom beams.

II. METHODS

The sketch of the studied system is presented in Fig. 1. The beam of ^{4}He projectiles with typical energies $E \sim 1$ keV is incident at LiF(001) surface at grazing polar angle Φ. Thus, the perpendicular to the surface motion of projectiles is slow, with corresponding momentum $k_\perp = k\sin(\Phi)$, and energy $E_\perp = E\sin^2(\Phi)$, where the total momentum is given by $k = \sqrt{2ME}$ and M is the projectile mass (we use atomic units through the text unless otherwise stated). The motion parallel to the surface is fast with momentum component $k_\parallel \sim k$, and energy $E_\parallel \sim E$. The beam is oriented at azimuthal angle Ψ measured with respect to the low index $\langle 110 \rangle$ direction at the surface. The diffracted beams leave the surface at azimuthal angles ψ_{mn} and polar angles ϕ_{mn}. The pair of indexes (m,n) defines the diffraction order as we discuss below.

In our experiments the primary He$^+$ ions are extracted at the desired energy from a commercial ion gun. They are neutralized in an effusive gas cell and resulting neutral fast ^{4}He atoms are drastically collimated before interacting with the surface in a UHV chamber at base pressure of some 10^{-11} mbar. The crystal surface is mounted with its normal direction aligned with that of the manipulator rotation axis allowing direct drive of the azimuth by a precision stepper motor with a single step sensitivity below 0.01°. The manipulator support flange can also be tilted with respect to the beam axis for the fine tuning of the incidence angle. The atoms reflected by the surface hit a microchannel plate amplifier stacked onto a phosphor screen located 740 mm downstream. The diffraction pattern is captured online by a CCD camera providing a pixel resolution of 4×10^{-3} deg. Each diffraction image provides

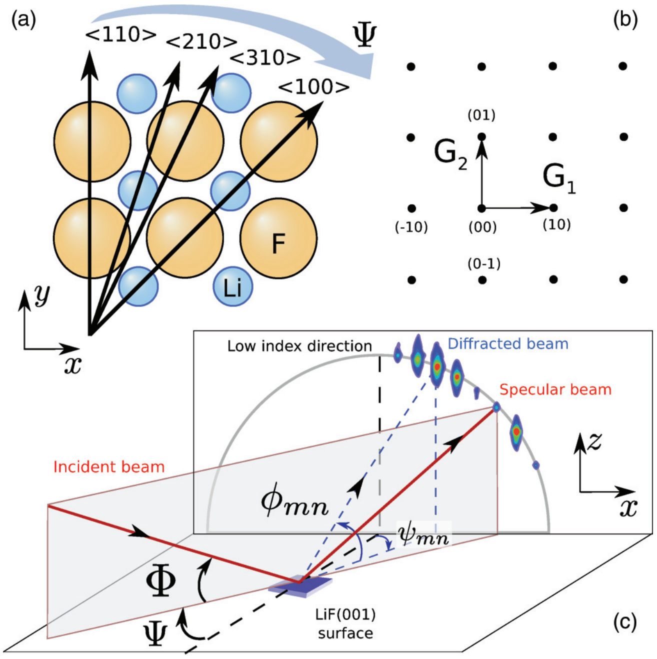

FIG. 1. (Color online) (a) Sketch of the LiF(001) surface. We use a coordinate system where y is along the $\langle 110\rangle$ direction. The most relevant low index directions are denoted by arrows. (b) Reciprocal two-dimensional (2D) surface lattice together with the primitive vectors. (c) Scattering geometry.

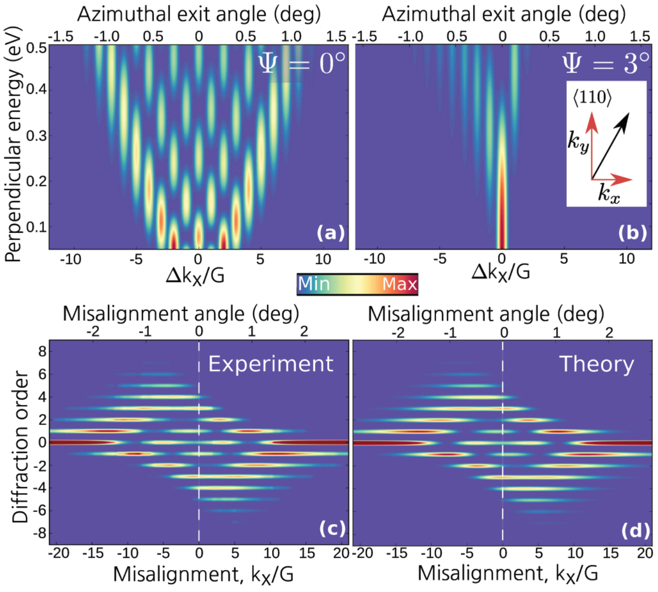

FIG. 2. (Color online) Diffraction charts for beams with total energy $E = 460$ eV. Topmost panels: Theoretical results for the diffraction as function of the incidence perpendicular energy $E_\perp$ and azimuthal exit angle (top axis) and momentum exchange Δk_x (bottom axis) are shown for (a) the perfectly aligned and (b) misaligned beam case. Bottom panels: Comparison between (c) experimental and (d) theoretical diffraction probability charts at $E_\perp = 120$ meV as function of the diffraction order and misalignment momentum (angle) denoted in the bottom (top) axis.

an independent absolute angular calibration: a fit through the coordinates of the primary (nonscattered) beam spot and those of the diffracted spots readily provides the coordinates of the Laue circle, i.e., its radius, and center related to the Φ and Ψ angles. This analysis yields an absolute accuracy in the 0.01° range. Finally, the LiF(001) sample was cleaved in air and rapidly introduced into the UHV chamber. A mild annealing to 500 K is sufficient to allow observation of intense and well-resolved diffraction patterns. Further details on our experimental procedure can be found elsewhere [6,7].

Present theoretical study is based on the time-dependent wave packet propagation (WPP) approach as developed for FAD [6,21,22]. The potential for He/LiF(001) projectile-surface interaction has been obtained from the quantum chemistry calculations [6] and was adjusted to include the effect of the surface rumpling [16]. From WPP we obtain the probabilities of the diffraction $\mathcal{R}_{mn}$ into the various (m,n) diffraction orders. The diffraction order is defined by the reciprocal lattice vector exchange with the surface such that parallel to the surface momentum component of the diffracted beam is given by $\mathbf{k}'_\parallel = \mathbf{k}_\parallel + m\mathbf{G}_1 + n\mathbf{G}_2$. The primitive reciprocal lattice vectors $\mathbf{G}_1$ and $\mathbf{G}_2$ of the LiF(001) surface are shown in Fig. 1. Their absolute values are $|\mathbf{G}_1| = |\mathbf{G}_2| = G$, where $G = 1.170 a_0^{-1}$. The diffracted beams leave the surface with perpendicular energies

$$E_\perp(m,n) = E_\perp - \frac{(m^2+n^2)}{2M}G^2 - \frac{(mk_x + nk_y)}{M}G, \quad (1)$$

where $k_x = k_\parallel \sin(\Psi)$, and $k_y = k_\parallel \cos(\Psi)$ [see Fig. 1(a)].

In practice, for small misalignment angles between the incident beam and $\langle \mu\nu 0\rangle$ low index direction at the surface, experimental and theoretical results show that the diffraction proceeds with reciprocal lattice vector exchange perpendicular to the $\langle \mu\nu 0\rangle$ direction. For example, for the ^{4}He beam oriented close to the $\langle 110\rangle$ direction at the LiF(001) surface, only the $(m,n=0)$ diffraction is possible and diffracted beams are located on the single Laue circle. Indeed the $n \neq 0$ diffraction is suppressed because it is associated with too large energy exchange between slow motion in the (x,z) plane and fast motion along the y coordinate [see Eq. (1)] [21,22]. The fast motion and slow motion appear decoupled so that one effectively deals with two-dimensional (2D) diffraction in the plane perpendicular to the surface. The fast projectiles "feel" the potential averaged along the axial channel, so that only surface corrugation across the channel is resolved [6,21,23]. This forms the basis for the 2D axial surface channeling (ASC) approximation in description of FAD experiments. It is worth noting, however, that recent results show the possibility of 3D diffraction for the reconstructed surfaces with large period along the fast motion direction [24,25].

III. RESULTS AND DISCUSSION

In Fig. 2 we show the calculated diffraction probabilities $\mathcal{R}_{m0}$ for the 460 eV ^{4}He beam incident close to the $\langle 110\rangle$ direction. The ASC approximation holds in this case and the diffraction process is fully determined by $E_\perp$, k_x, and the momentum change in x direction $\Delta k_x = mG$. In Figs. 2(a) and 2(b) theoretical results are then shown as function of $E_\perp$ and Δk_x for fixed values of k_x given by the beam misalignment angle. In Figs. 2(c) and 2(d) experimental and theoretical data are presented as function of misalignment k_x and diffraction order ($m = \Delta k_x/G$) for fixed value of $E_\perp = 120$ meV. Artificial broadening in Δk_x is applied to the theoretical data to mimic the experimental broadening effects. Note that while the diffraction probabilities are independent of the fast motion along the $\langle 110\rangle$ direction, the latter defines the geometrical characteristics of the process such as the azimuthal exit angles of the diffracted beams: $\tan(\psi_{mn}) = (k_x + mG)/k_y$.

For the perfectly aligned beam with $\Psi = 0^\circ$ the symmetric diffraction pattern as obtained in Fig. 2(a) is in full accord with earlier published results [5,6,10]. For each $E_\perp$ energy, the range of the $\psi_{m,n=0}$ angles contributing to the diffraction pattern is bounded by the rainbow angles Ψ_R, corresponding to the maximum azimuthal scattering angles attained classically. The diffracted beams leaving the surface close to the rainbow angle are most intense reflecting the classical divergence of the scattering intensity at Ψ_R [26]. With increasing misalignment Ψ, the diffraction pattern becomes asymmetric as shown in Fig. 2(b). For $\Psi > 0$, there is less diffracted beams with $m > 0$ as compared to $m < 0$ beams. Indeed, the diffraction with $m > 0$ is reduced because it corresponds to larger final momentum along the x axis and to larger change of the perpendicular energy $E_\perp(m,0) - E_\perp$ [22]. Thus, the reciprocal lattice vectors are preferentially exchanged in the direction opposite to k_x [20]. For large misalignment angles Ψ the energy exchange between parallel and perpendicular to the surface motion given by Eq. (1) is too large. The diffraction pattern shrinks and eventually only specular reflection is observed [10,19].

Figures 2(c) and 2(d) extend the analysis of the characteristic asymmetry of the diffraction pattern upon misalignment of the incident beam (see also Refs. [19,20]). At that point we underline the excellent agreement between calculated and measured diffraction probabilities. This is while the calculations are performed for the perfect rigid surface and experimental data is affected by inelastic and further decoherence processes. These are present and increase in magnitude with increasing momentum exchange between the projectile and the surface. The diffraction pattern gradually evolves from well-defined spots located on the Laue circle [see Fig. 1(c)] to stripes elongated in the z direction together with a progressive broadening along the x direction. The experimental results shown in this paper are obtained with low incidence angles ($\lesssim 1^\circ$) where well resolved diffraction peaks are observed from which the full intensity has been extracted. It follows from Figs. 2(c) and 2(c) that for positive (negative) misalignment diffraction orders with negative (positive) m prevail. That is, diffraction with $mk_x < 0$ dominates, and the flux of outgoing particles is preferentially distributed among diffraction orders pointing in the direction of the axial channel. In overall the k_x momentum component is reduced, and the outgoing beam appears deflected from the specular direction towards the low index direction at the surface. It is noteworthy that the average outgoing polar angle will be in this case larger than Φ since for $mk_x < 0$, Eq. (1) gives $E_\perp(m,0) > E_\perp$. Observe that the maximum momentum exchange $\Delta k_x = \mp 5G$ is reached at misalignment $k_x = \pm 5G$ close to the rainbow angle. It corresponds to the diffracted beam leaving the surface perfectly aligned with the $\langle 110\rangle$ direction. Similar results are obtained for the incident beam oriented close to the $\langle 100\rangle$ direction.

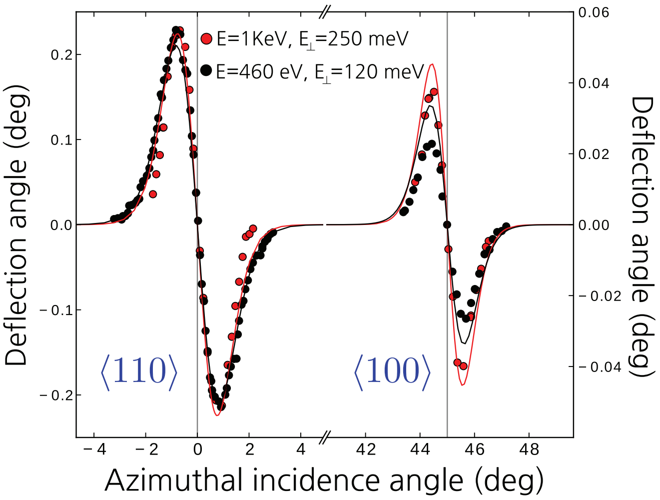

FIG. 3. (Color online) Mean deflection angle as function of the azimuthal incidence angle. Experimental results (dots) for two scattering conditions (see legend) are compared with theoretical calculations (solid lines). The left (right) axis corresponds to the $\langle 110\rangle$ ($\langle 100\rangle$) direction denoted by a vertical line.

Let us introduce a classical measure of the asymmetry of the diffraction pattern. It is given by the mean (azimuthal) deflection angle defined as $\Omega = \overline{\psi} - \Psi$ with

$$\overline{\psi} = \sum_{m,n}^{\text{open}} \mathcal{R}_{mn}\psi_{mn}, \qquad (2)$$

where the summation runs over all open diffraction orders with $E_\perp(m,n) > 0$ [see Eq. (1)]. Provided the validity of the ASC approximation, Ω is intimately linked with the mean momentum exchange perpendicular to the low index direction [20]. With present definitions of geometry, and for scattering close to the $\langle 110\rangle$ direction, one has $\overline{\psi} \approx \overline{m}G/k_\parallel$, where $\overline{m} = \sum_m^{\text{open}} m\mathcal{R}_{m0}$. Basically, $\overline{m}$ is the mean of the distribution given by the data shown in Figs. 2(c) and 2(d) taken along the vertical line at fixed k_x.

In Fig. 3 we show measured and calculated mean deflection angle Ω as function of the azimuthal incidence angle Ψ for the ^{4}He beam incident at LiF(001) surface. The Ψ range displayed here covers two main low index directions, and the rest of the data can be obtained by symmetry considerations. The two data sets displayed in Fig. 3 correspond to different incidence conditions as specified in the legend. Experimentally, the mean deflection angle is obtained with Eq. (2) using fitted intensities of the diffraction orders. The associated statistical error is below 0.01°, however the result is easily affected by systematic errors due to detector inhomogeneity, background noise level, and chosen boundaries of the diffraction spots. The precise determination of these has not been attempted in this work. This being said, we believe that the present level of precision is enough for the purpose of the paper. Interestingly, we have found that $\overline{\psi}$ can also be accurately estimated with a simple running average through all the pixels of the diffraction

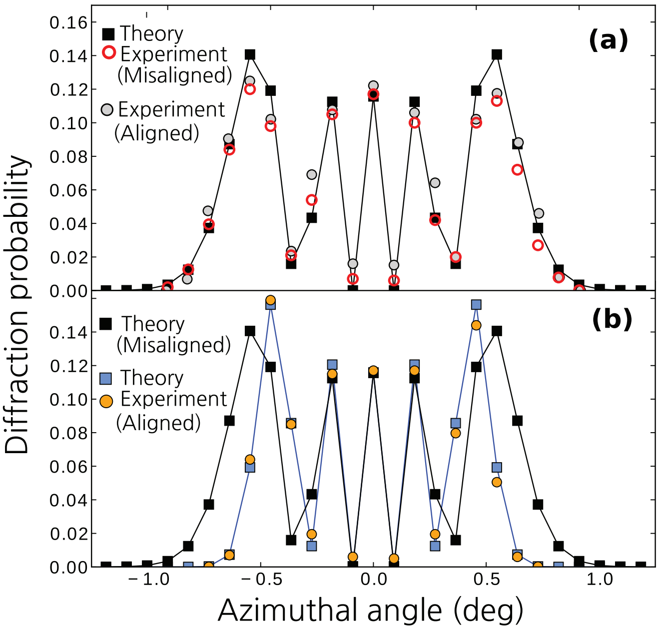

FIG. 4. (Color online) Illustration of the detailed balance principle for the diffraction of the 1 keV ^{4}He beam incident close to the $\langle 110\rangle$ direction at the LiF(001) surface. (a) Probability of the perfectly aligned exit (along the axial channel) as function of the azimuthal *misalignment* incidence angle Ψ with $E_\perp = 250$ meV. Results are compared with the inverse scattering process where the incident beam is *aligned* and energy corrected (see main text). (b) Comparison of the probability of aligned exit for misaligned incidence shown as function of the misalignment incidence angle, and $\mathcal{R}_{m0}$ diffraction probabilities for the incidence along the $\langle 110\rangle$ direction (aligned). $\mathcal{R}_{m0}$ are plotted as function of the azimuthal exit angles ψ_{m0} with $E_\perp = 250$ meV.

patterns. This latter treatment can be performed online and, for example, inserted in a control loop for automated target positioning.

In agreement with data shown in Figs. 2(c) and 2(d), for large misalignment from the low index direction the incident beam is specularly reflected at the surface so that no deflection occurs ($\Omega = 0$). As the orientation of the beam Ψ approaches the low index $\langle \mu\nu 0\rangle$ direction at the azimuth angle $\Psi_{\langle \mu\nu 0\rangle}$, the mean deflection angle shows a characteristic dependence with misalignment: (i) The mean deflection angle is positive $\Omega > 0$ for $\Psi - \Psi_{\langle \mu\nu 0\rangle} < 0$, (ii) no deflection occurs for the perfectly aligned beam with $\Omega = 0$, and (iii) Ω turns negative for $\Psi - \Psi_{\langle \mu\nu 0\rangle} > 0$. The misalignment is thus reduced in the scattered beam, which is deflected towards the closest low index direction. With the present incidence conditions the mean deflection angle can reach 0.22°. However, Ω is always smaller than the misalignment with, in overall, $\Omega \sim -0.38(\Psi - \Psi_{\langle 110\rangle})$ and $\Omega \sim -0.09(\Psi - \Psi_{\langle 100\rangle})$ in the small misalignment range close to the low index direction where the linear relation holds. Due to the larger surface corrugation probed by the projectiles, the deflection for the $\langle 110\rangle$ axial channel is larger than for the $\langle 100\rangle$ channel. It is also interesting to mention that the characteristic dependence of the mean deflection angle on the azimuthal misalignment provides an alternative way of the Ψ angular calibration. Indeed, even if the calibration of angles is wrong (or unknown), the $\Omega(\Psi)$ curves measured near the main symmetry directions cross zero with a steep slope allowing to relate Ψ with crystallographic directions at the surface.

The largest deflection is reached at the optimum misalignment incidence angle close to the rainbow angle Ψ_R. Indeed, for the aligned beam Ψ_R is the maximum azimuthal diffraction angle that carries high intensity of the outgoing beam. From the principle of detailed balance [27] it follows that the maximum misalignment angle at which the incident beam is efficiently deflected into the direction of the axial channel is also given by Ψ_R. Indeed, the probability of the diffraction with $\mathbf{k}_\parallel \to \mathbf{k}'_\parallel = \mathbf{k}_\parallel + m\mathbf{g}_1 + n\mathbf{g}_2$ equals to the probability of the inverse process $\mathbf{k}'_\parallel \to \mathbf{k}_\parallel = \mathbf{k}'_\parallel - m\mathbf{g}_1 - n\mathbf{g}_2$, where both processes are considered at the fixed total energy E. Let $\mathcal{R}_{mn}$ to describe the diffraction probability for the beam incident at the surface along the $\langle \mu\nu 0\rangle$ low index direction with total energy E and perpendicular energy $E_\perp$. The corresponding diffracted beam leaves the surface at azimuthal angle ψ_{mn} with perpendicular energy $E_\perp(m,n)$. From the detailed balance principle it follows then that $\mathcal{R}_{mn}$ also describes the probability of perfectly aligned exit for the beam incident with misalignment angles $\Psi = \pm\psi_{mn}$, total energy E, and perpendicular energy $E_\perp(m,n)$. Obviously, the largest $\mathcal{R}_{mn}$ correspond to the rainbow angles.

In Fig. 4 the above discussion is illustrated with experimental and theoretical data for the ^{4}He beam incident close to the $\langle 110\rangle$ direction at LiF(001) surface. In Fig. 4(a) we show the probability of the perfectly aligned exit (along the axial channel) as function of the incident beam azimuthal misalignment angle Ψ. The perpendicular energy of the incident beam is 250 meV. The perfect alignment of the $(-m,0)$ diffracted beams with $\psi_{-m0} = 0$ is only possible at discrete misalignment incidence angles $\Psi_m = \arcsin(mG/k_\parallel)$ such that $k_x = mG$. The perfectly aligned beam leaves the surface with perpendicular energy $E_\perp(m,0) = 250\ \text{meV} + (mG)^2/2M$ as follows from Eq. (1). We also show the experimental data obtained with perfectly aligned beam for the probability of the diffraction into the $(m,0)$ diffraction orders. Results are shown as function of the outgoing azimuthal angle $\psi_{m0} = \arcsin(mG/k_\parallel)$. To comply with the detailed balance, the intensity of each diffraction order has been measured at the particular perpendicular energy $E_\perp = E_\perp(m,0)$, while keeping the total energy fixed. The data sets obtained with misaligned and aligned beams coincide. Interestingly, Fig. 4(a) demonstrates that with detailed balance principle, the diffraction charts obtained with perfectly aligned beams can be reconstructed from the data on the aligned exit as function of the beam misalignment.

Finally, Fig. 4(b) demonstrates the importance of the perpendicular energy correction. Theoretical results obtained for the probability of aligned exit with misaligned beam at $E_\perp = 250$ meV [same as in Fig. 4(a)] are compared with calculated and measured probabilities of the diffraction for the perfectly aligned beam with $E_\perp = 250$ meV. While for small reciprocal lattice vector exchange the perpendicular energy correction is not important and all data sets coincide, for large reciprocal vector exchange the data sets obtained with aligned and misaligned beams at fixed perpendicular energy differ.

IV. SUMMARY AND CONCLUSION

In summary, with the example of ^{4}He scattering from the LiF(001) surface, we demonstrated controllable surface deflection of fast atom beams at grazing incidence geometry. When the incident beam is misaligned with respect to the low index direction, atomic rows guide the projectiles leading to the characteristic deformation of the diffraction pattern and overall deflection of the beam in the direction of the axial channel. For small misalignments, the mean deflection angle Ω is proportional to the misalignment angle Ψ with $\Omega \approx 0.1\Psi - 0.4\Psi$. The largest deflection is achieved for the azimuthal misalignment angles equal to the rainbow angle ψ_R for the perfectly aligned beam, and deflection efficiency drops for higher misalignments. Thus the 2D grazing scattering at monocrystal surfaces can be used for the deflection of fast projectile beams, similar to the 3D guiding of swift projectiles channeling through bent monocrystals as used in high-energy physics [28–30]. Importantly, for small incidence angles a large fraction of the diffracted beams preserve quantum coherence. The results of our study thus suggest that surface scattering at grazing angles can be used for coherent manipulation of fast atom beams. For example, incidence of two coherent misaligned beams with $\Psi = \pm\Psi_R$ can allow for efficient coherent beam combining into the beam aligned along the axial channel.

ACKNOWLEDGMENT

This work has been funded by the French Agence Nationale de la Recherche (ANR-2011-EMMA-003-01).

[1] K. J. Snowdon, D. J. O'Connor, and R. J. MacDonald, Phys. Rev. Lett. **61**, 1760 (1988).

[2] D. M. Goodstein, R. L. McEachern, and B. H. Cooper, Phys. Rev. B **39**, 13129 (1989).

[3] H. Niehus, W. Heiland, and E. Taglauer, Surf. Sci. Rep. **17**, 213 (1993).

[4] H. Winter, Phys. Rep. **367**, 387 (2002).

[5] A. Schüller, S. Wethekam, and H. Winter, Phys. Rev. Lett. **98**, 016103 (2007).

[6] P. Rousseau, H. Khemliche, A. G. Borisov, and P. Roncin, Phys. Rev. Lett. **98**, 016104 (2007).

[7] N. Bundaleski, H. Khemliche, P. Soulisse, and P. Roncin, Phys. Rev. Lett. **101**, 177601 (2008).

[8] J. Seifert, A. Schüller, H. Winter, R. Włodarczyk, J. Sauer, and M. Sierka, Phys. Rev. B **82**, 035436 (2010).

[9] A. Schüller, M. Busch, S. Wethekam, and H. Winter, Phys. Rev. Lett. **102**, 017602 (2009).

[10] H. Winter and A. Schüller, Prog. Surf. Sci. **86**, 169 (2011).

[11] J. R. Manson, H. Khemliche, and P. Roncin, Phys. Rev. B **78**, 155408 (2008).

[12] F. Aigner, N. Simonović, B. Solleder, L. Wirtz, and J. Burgdörfer, Phys. Rev. Lett. **101**, 253201 (2008).

[13] J. Lienemann, A. Schüller, D. Blauth, J. Seifert, S. Wethekam, M. Busch, K. Maass, and H. Winter, Phys. Rev. Lett. **106**, 067602 (2011).

[14] J. Seifert and H. Winter, Phys. Rev. Lett. **108**, 065503 (2012).

[15] J. Seifert and H. Winter, Surf. Sci. **610**, L1 (2013).

[16] A. Schüller, S. Wethekam, D. Blauth, H. Winter, F. Aigner, N. Simonović, B. Solleder, J. Burgdörfer, and L. Wirtz, Phys. Rev. A **82**, 062902 (2010).

[17] M. S. Gravielle and J. E. Miraglia, Phys. Rev. A **78**, 022901 (2008).

[18] M. S. Gravielle, A. Schüller, H. Winter, and J. E. Miraglia, Nucl. Instrum. Methods Phys. Res. Sect. B **269**, 1208 (2011).

[19] J. Seifert, A. Schüller, H. Winter, and K. Gärtner, Nucl. Instrum. Methods Phys. Res. Sect. B **269**, 1212 (2011).

[20] A. Ruiz, J. P. Palao, and E. J. Heller, Phys. Rev. A **79**, 052901 (2009).

[21] A. Zugarramurdi and A. G. Borisov, Phys. Rev. A **86**, 062903 (2012).

[22] A. Zugarramurdi and A. G. Borisov, Phys. Rev. A **87**, 062902 (2013).

[23] D. Farías, C. Díaz, P. Nieto, A. Salin, and F. Martín, Chem. Phys. Lett. **390**, 250 (2004).

[24] M. Busch, J. Seifert, E. Meyer, and H. Winter, Phys. Rev. B **86**, 241402 (2012).

[25] A. Zugarramurdi and A. G. Borisov, Nucl. Instrum. Methods Phys. Res. Sect. B, doi: 10.1016/j.nimb.2013.02.007.

[26] S. Miret-Artés and E. Pollak, Surf. Sci. Rep. **67**, 161 (2012).

[27] A. Bohm, *Quantum Mechanics: Foundations and Applications* (Springer-Verlag, Berlin, 1993).

[28] Yu. M. Ivanov *et al.*, Phys. Rev. Lett. **97**, 144801 (2006).

[29] W. Scandale *et al.*, Phys. Rev. Lett. **98**, 154801 (2007).

[30] W. Scandale *et al.*, Phys. Rev. Lett. **101**, 164801 (2008).